Optical Properties of Bulk High-Entropy Diborides for Solar Energy Applications

[1]Simone Barbarossa, [1,*]Roberto Orrù, [1]Giacomo Cao,

[2]Andrea Balbo, [2]Federica Zanotto, [3]Elisa Sani

[1]Dipartimento di Ingegneria Meccanica, Chimica, e dei Materiali, Unità di Ricerca del Consorzio Interuniversitario Nazionale per la Scienza e Tecnologia dei Materiali (INSTM), Università degli Studi di Cagliari, via Marengo 2, 09123 Cagliari, Italy

[2]Corrosion and Metallurgy Study Centre "Aldo Daccò", Engineering Department, University of Ferrara, G. Saragat 4a, Ferrara 44122, Italy

[3]CNR-INO National Institute of Optics, Largo E. Fermi, 6, I-50125 Firenze, Italy

https://doi.org/10.1016/j.jallcom.2022.167965

Abstract

So far, the studies regarding the innovative High-Entropy Borides (HEBs), which belong to the more general class of Ultra-high temperature ceramics (UHTCs), have been entirely confined to their fabrication or characterization from the microstructural, mechanical and oxidation resistance viewpoints.

In this work, the optical properties of two members of HEBs, i.e. $(Hf_{0.2}Zr_{0.2}Ta_{0.2}Mo_{0.2}Ti_{0.2})B_2$ and $(Hf_{0.2}Nb_{0.2}Ta_{0.2}Mo_{0.2}Ti_{0.2})B_2$, are evaluated for the first time to assess their possible utilization in the thermal solar energy field. The bulk samples (96.5 and 97.4% dense, respectively) are obtained as single-phase products by Spark Plasma Sintering (1950 °C/20 min/20 MPa) starting from powders previously synthesized by Self-propagating High-temperature Synthesis (SHS). The optical characterization, whose results are discussed by comparing HEBs to the individual borides, shows that they are characterized by intrinsic spectral selectivity and low thermal emittance, resulting therefore interesting for high-temperature solar absorbers applications.

(*) Corresponding author, email: roberto.orru@unica.it

Keywords: Ultra High Temperature High-Entropy Ceramics; Spark Plasma Sintering; Optical properties; Solar absorbers; Solar plants; Concentrated solar power.

1. Introduction

The recently discovered class of ultra-refractory ceramics referred to as High Entropy Borides (HEBs) is obtained by the combination, in near-atomic ratio, of usually five transition metal elements uniformly distributed across the boride lattice, to produce single-phase crystalline solid solutions with maximum configurational entropy **[1-6]**. Examples of these ceramics are $(Hf_{0.2}W_{0.2}Ta_{0.2}Zr_{0.2}Ti_{0.2})B_2$, $(Hf_{0.2}Mo_{0.2}Ta_{0.2}Zr_{0.2}Ti_{0.2})B_2$, $(Hf_{0.2}Ta_{0.2}Zr_{0.2}Nb_{0.2}Ti_{0.2})B_2$, etc.

Since their discovery, the first target has been the identification of convenient synthesis/consolidation routes to produce highly dense and homogeneous ceramics with no undesired secondary phases. In this regard, powders preparation is usually carried out by borothermal/boro-carbothermal reduction **[4,7-9]** or self-propagating high temperature synthesis (SHS) **[2,3,10]** processes. On the other hand, the Spark Plasma Sintering (SPS) technology is unequivocally the main consolidation techniques adopted to provide dense HEBs **[1-4,7-11]**.

The resulting materials need to be subjected to an extensive characterization to evaluate their performances when subjected to conditions required by specific industrial applications, and finally their behavior is compared with that of standard individual diborides. Along this line, the studies carried out up to now refers to mechanical **[1,8-11],** thermal conductivity **[8,12]** and oxidation resistance **[1,13,14]** properties.

In this context, to the best of our knowledge, only two studies **[15,16]** have been carried out so far to determine the optical properties of this emerging class of ceramics, which might be, as for the case of standard Ultra-High Temperature Ceramics (UHTCs), promising for their potential utilization in the thermal solar energy field. Both these investigations were focused on the fabrication as coatings, and their optical characterization, of high-entropy alloy nitrides (HEANs), namely AlCrWTaNbTiN **[15]** and AlCrTaTiZrN **[16]**. AlCrWTaNbTiN-based solar selective absorbing coatings were found to provide a high solar absorptance (0.93) and a low thermal emittance (0.068, at 82 °C) **[15]**. Similarly, the AlCrTaTiZrN-based coating was reported to show excellent optical performance, with solar absorptance of 0.965, and a thermal emittance of 0.086 **[16]**.

In spite of the several studies conducted in the literature involving binary diborides (ZrB_2, TaB_2, HfB_2, TiB_2, etc.) to be used as solar receivers either in bulk **[17-22**] or in coating forms **[23-27]**, the optical properties of HEBs are totally unexplored.

UHTCs based on transition metal borides have attracted a significant attention in the last decade as potential candidates for innovative solar absorbers able to operate at very high temperatures **[28]**. Such interest is due to their favorable optical and radiative properties like intrinsic spectral selectivity and low thermal emittance. It is worth to recall that the increase of the operating temperature of concentrating solar

energy systems is a key technological improvement both to boost the efficiency of thermodynamic cycles for power production and to disclose novel emerging applications of so-called Concentrating Solar Thermal (CST). The supply of high-temperature solar heat to energy-intensive industries (e.g. cement, glass, foundry, etc.) determines a reduction of the carbon footprint of those industrial sectors, which, according to IRENA, are the largest CO_2 emitters and the most difficult to decarbonize **[29]**. Furthermore, two remarkable recent examples of CST applications can be found in the green production of hydrogen **[30]** and sustainable aviation fuels (SAF) **[31]**. They consist in the production of fuels from water and CO_2 through endothermic reactions at high temperatures driven by solar heat. This approach, which effectively would close the fossil fuel carbon cycle **[32]**, requires temperatures from above 700 °C up to ~1550 °C. These solar-driven chemical processes show an outstanding potential. For instance, they are thought to be able to supply the whole global demand of jet fuels **[33,34]**, thus significantly decreasing both the global dependence from fossil fuels and the greenhouse emissions.

Within this framework, in the present work we report on the successful synthesis of two bulk ceramic systems consisting of $(Hf_{0.2}Zr_{0.2}Ta_{0.2}Mo_{0.2}Ti_{0.2})B_2$ and $(Hf_{0.2}Nb_{0.2}Ta_{0.2}Mo_{0.2}Ti_{0.2})B_2$, respectively, and their optical properties measured in the range from 0.3 to 16 μm wavelength, to evaluate the materials' interaction with both solar and thermal radiation. Both ceramics are first prepared by the SHS-SPS method and characterized from the compositional, microstructural, and textural points of view. From experimental optical spectra, solar absorptance and thermal emittance up to ~2000°C (1700K) are then estimated. Optical properties and optical parameters are finally discussed and compared to those of the individual monolithic borides.

2. Experimental Materials and Methods

2.1. Synthesis and consolidation of High-Entropy Borides

According to the SHS-SPS processing route, the obtainment of bulk $(Hf_{0.2}Zr_{0.2}Ta_{0.2}Mo_{0.2}Ti_{0.2})B_2$ (labelled as HEB_Zr) and $(Hf_{0.2}Nb_{0.2}Ta_{0.2}Mo_{0.2}Ti_{0.2})B_2$ (labelled as HEB_Nb) specimens by SPS is preceded by the synthesis of related powders via SHS. To this aim, depending on the specific HEB system to be synthesized, Hf (Alfa Aesar, cod. 00337, particle size < 44 μm, 99.6 % purity), Mo (Aldrich, cod 266892, particle size < 149 μm, 99% purity), Ta (Alfa Aesar, cod 00337, particle size < 44 μm, 99.9 % purity), Nb (Alfa Aesar, cod 010275, particle size < 44 μm, 99.8 % purity), Ti (Aldrich, cod 268496, particle size < 149 μm, 99.7 purity), Zr (Alfa Aesar, cod 00418, particle size < 44 μm, > 98.5 % purity), and B (Aldrich, cod 15580, amorphous, 99 % purity) precursors are first dry mixed in stoichiometric proportions, as far as metal constituents are concerned, whereas boron is used in slight excess (B to metal ratio equal to 2.2:1). Indeed, as explained elsewhere **[18,35]**, part of this element is consumed by the borothermal reduction of oxide impurities originally present in raw powders as well as by volatilization phenomena occurring during the synthesis process. Mixed powders are then cold pressed to form cylindrical pellets that are locally ignited under Argon environment using a heated filament.

The obtained combustion synthesized samples are preliminarily ball milled for 60 min (SPEX CertiPrep, USA, charge ratio equal to 2) to convert them in powder form before being consolidated by SPS (515S model equipment, Fuji Electronic Industrial Co., Ltd., Kanagawa, Japan). SHS powders are processed by SPS once mixed with 1.0 wt.% of graphite (Aldrich, cod 282863, particle size < 20 μm). This is because, as shown elsewhere **[3]**, the introduction of this additive allows for the removal of residual oxides impurities and the concurrent improvement of powder densification. Sintering experiments are conducted in vacuum conditions under temperature-controlled mode using an infrared pyrometer (CHINO, mod. IR-AHS2, Japan) focused on the external surface of a cylindrical die (30 mm external diameter; 15 mm inside diameter; 30 mm height) consisting of graphite (AT101, ATAL Srl, Italy). All the samples considered in the present work for optical characterization are prepared as follows. During SPS experiments, temperature is first increased in 10 min to 1950°C (T_D), then maintained for 20 min at the latter value and, finally, decreased down to the room temperature. The sintering process was entirely conducted under 20 MPa of mechanical pressure. Sample's release is made easier using graphite foils (99.8 % pure, 0.13 mm thick, Alfa Aesar, Karlsruhe, Germany) to separate internal surfaces of the die, the top and bottom sides of the punches, from powders undergoing sintering. In addition, the die was

surrounded with a layer of graphite felt to minimize heat losses by radiation. For the sake of reproducibility, each experimental condition was repeated at least twice.

Absolute samples' density was determined by the Archimedes' method with distilled water as immersion medium. The corresponding relative values were calculated by considering 8.52 and 8.67 g/cm^3 as theoretical densities of $(Hf_{0.2}Zr_{0.2}Ta_{0.2}Mo_{0.2}Ti_{0.2})B_2$ and $(Hf_{0.2}Nb_{0.2}Ta_{0.2}Mo_{0.2}Ti_{0.2})B_2$, respectively **[1]**. The presence of graphite (ρ = 2.26 g/cm^3) was properly considered using a mixing rule for the evaluation of corresponding relative densities **[36]**.

Before microstructural and optical characterization, the sample surfaces were mechanically lapped with progressively finer emery paper up to P4000 (FEPA standard 43-GB-1984), to finally obtain about 3 mm thick disks.

2.2. Microstructural and topological characterization

Crystalline phases present on the samples surface were identified by X-ray diffraction analysis (Ni filtered CuKα radiation, Philips PW 1830, Netherlands) over a range of scattering angles 2ϑ from 25° to 100°, in steps of 0.05° with 15 s acquisition time per angle.

The microstructural characteristics and the surface morphology were investigated by a scanning electron microscope (SEM, Zeiss EVO MA15, Zeiss, Oberkochen, Germany), operating at 20 kV. SEM micrographs were processed by using an image analysis software for a quantitative measurement.

Surface texture analysis was performed with a noncontact optical profilometer (Taylor-Hobson CCI MP, Leicester, UK) equipped with a green light and a 20X magnification objective lens.

Four distinct areas were analyzed for each specimen, and the collected surface data were processed with the Talymap 6.2 software (Taylor-Hobson, Leicester, UK) to extract 3D areal field parameters.

The average 3D texture parameters were obtained following the ISO 25178-2:2012 standard on S-F surfaces, after denoising (median filter 5 × 5), form removing and S-filter application.

2.3. Optical properties

Hemispherical reflectance spectra were acquired using a double-beam spectrophotometer (Lambda900 by Perkin Elmer) with Spectralon®-coated integration sphere for the 0.3 – 2.5 μm wavelength region and a Fourier Transform spectrophotometer (FT-IR "Excalibur" by Bio-Rad) with gold-coated integrating sphere and liquid nitrogen-cooled detector for the range 2.5 – 16.0 μm. From

experimental reflectance data ($R^{\cap}(\lambda)$), the spectral absorbance $\alpha(\lambda)$ or emittance $\varepsilon(\lambda)$ of these fully opaque materials can be obtained, as:

$$\alpha(\lambda)= 1-R^{\cap}(\lambda)= \varepsilon(\lambda) \qquad (1)$$

From experimental spectra, it is possible to calculate some parameters useful to evaluate the potential of the materials as sunlight absorbers in solar receivers for thermodynamic solar plants, namely the solar absorptance α, the total hemispherical emittance ε at the temperature T, and the spectral selectivity α/ε, as follows:

$$\alpha = \frac{\int_{0.3\mu m}^{3\mu m} \alpha(\lambda)\cdot S(\lambda) d\lambda}{\int_{0.3\mu m}^{3\mu m} S(\lambda) d\lambda} \qquad (2)$$

$$\varepsilon = \frac{\int_{0.3\mu m}^{16.0\mu m} \varepsilon(\lambda)\cdot B(\lambda,T) d\lambda}{\int_{0.3\mu m}^{16.0\mu m} B(\lambda,T) d\lambda} \qquad (3)$$

where S(λ) is the sunlight spectral distribution **[37]** and B(λ,T) is the blackbody spectral radiance at the temperature T. For a more complete evaluation, the emittance in Eq. 3 has been calculated at different temperatures from 800 K to 1700 K. As a methodology comment referred to these parameters, it should be observed that the values calculated from Eqs. 1 – 3, being obtained from room-temperature spectra, represent an estimation widely used in the literature for a comparative evaluation among materials, while they cannot represent exact values in operative conditions, which would need the knowledge of the spectra at the considered temperature, and result generally underestimated **[38]**.

3. Results and discussion

3.1. Products density and composition

The self-propagating reactions for the synthesis of $(Hf_{0.2}Zr_{0.2}Ta_{0.2}Mo_{0.2}Ti_{0.2})B_2$ and $(Hf_{0.2}Nb_{0.2}Ta_{0.2}Mo_{0.2}Ti_{0.2})B_2$ from elemental powders lead to multiphases ceramics **[3,10]**. The SHS products were ball milled for 60 min and particle size data of the resulting powders, measured by laser light scattering analysis, are summarized in **Table 1**. Comparable results are obtained for the two groups of powders, although HEB_Zr particles are slightly finer.

Table 1. Particle size parameters of HEB powders synthesized by SHS after being ball milled for 1 h prior SPS.

System	d_{10} (μm)	d_{50} (μm)	d_{90} (μm)	d_{av}(μm)
HEB_Zr	0.25	1.29	8.49	2.93
HEB_Nb	0.16	1.13	11.69	3.69

When these powders are subsequently processed by SPS under convenient conditions, the resulting bulk products basically consist of the desired high-entropy phases only. This statement is clearly supported by XRD analysis carried out on the optically-prepared surfaces (**Figure 1**). In this regard, it should be noted that detailed previous analysis carried out on the cross sections of graphite-free samples revealed the presence of metal oxide contaminants (8.8 and 2.2 wt.%, for the case of HEB_Zr and HEB_Nb systems, respectively) **[3]**. However, as mentioned in section 2.1, such impurities can be significantly abated with the graphite introduction (to 0.5 and 0.2 wt.%, respectively), due to their carbothermal reduction. **Barbarossa et al. [3]** also evidenced that about 70 and 90 wt.%, depending on the system, of graphite initially added to the SHS powders before SPS was still found in sintered samples, to indicate that only a small amount of additive was consumed for oxides elimination. Nonetheless, the graphite percentage chosen in this work (1 wt.%) was found to be the optimal one to maximize the other concurrent relevant effect, i.e., the marked powder densification improvement, i.e. from 87±0.7 to 96.5±0.7 % (HEB_Zr) and from 92.5±1.3 to 97.4±0.3% (HEB_Nb) **[3,10].** Indeed, it is well recognized that the presence of O-impurities hinders powder consolidation, so that their removal is beneficial to make powders more reactive and sinterable **[3,39]**. In addition, it was postulated that graphite also acts as a solid lubricant, which provides a supplementary contribution to provide ultra-high-temperature ceramics with higher relative densities **[40]**.

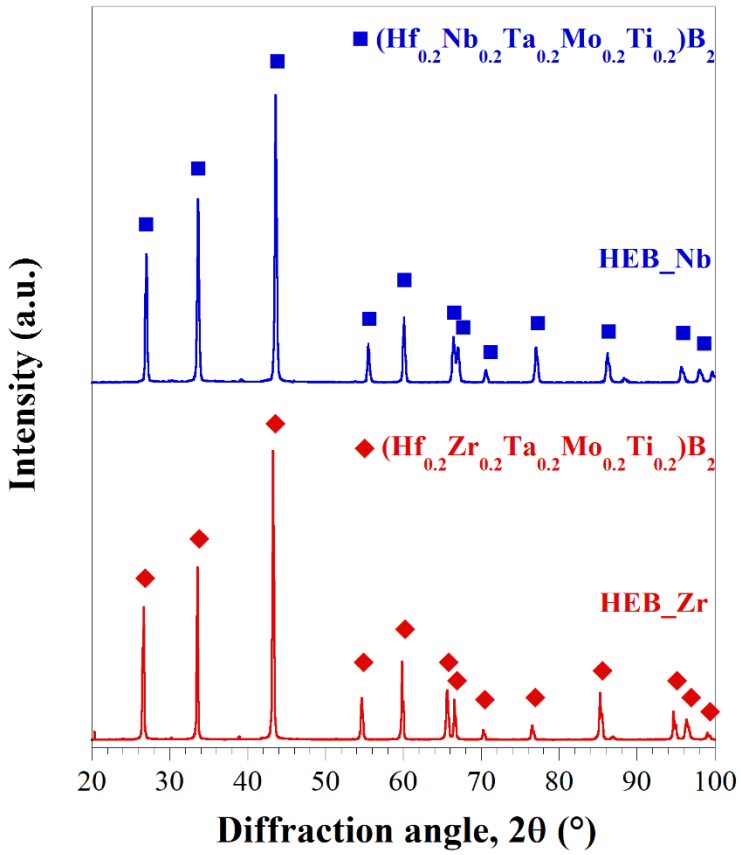

Figure 1. XRD patterns relative to the surface of bulk $(Hf_{0.2}Zr_{0.2}Ta_{0.2}Mo_{0.2}Ti_{0.2})B_2$ (HEB_Zr) and $(Hf_{0.2}Nb_{0.2}Ta_{0.2}Mo_{0.2}Ti_{0.2})B_2$ (HEB_Nb) sintered samples obtained by SPS (1950°C, 20 min, 20 MPa) in presence of 1.0 wt.% graphite

3.2. Microstructure

Figure 2 shows the microstructure of HEB_Zr and HEB_Nb samples after densification and mechanical surface polishing. Both systems show a quite homogeneous microstructure characterized by equiaxial grains with average sizes of 5.4 ± 2.0 μm and 10.9 ± 4.6 μm for HEB_Zr and HEB_Nb, respectively.

A small volume fraction of residual porosity, mainly located at grain boundary, was observed in both systems (i.e., 2.3vol% and 1.5vol % for HEB_Zr and HEB_Nb, respectively) with average pore size of about 0.5 μm (**Table 2**).

Despite the same densification process conditions are adopted (1950°C, 20 min, 20 MPa), the HEB_Zr sample shows lower grain size and slightly higher amount of residual porosity. The first issue might be due to the relatively finer particles undergoing SPS for this system (**Table 1**). In addition, the motivation

for the observed different porosity could be the relatively larger content of residual oxides detected in HEB_Zr (0.5 wt.%) compared to HEB_Nb (0.2 wt.%). Indeed, as mentioned previously, the presence of such impurities is well known to inhibit powder consolidation.

In the latter regard, literature data highlighted that the addition of transition metals can affect both densification and grain growth of diboride ceramics. In particular, it has been observed that an increase of Nb content gives rise to reduced grains size **[4,41]**. The results presented here suggest that the addition of Zr has a similar effect, being even more effective than Nb in the grain growth suppression. It is presumable that the presence of the highly refractory Zr element could play a role in making relatively finer microstructures.

Table 2. Characteristics of HEB samples investigated in the present work. Data of previously investigated binary borides produced by SHS-SPS, except for HfB_2 (reactive SPS), are also listed, for comparison. n.r. not reported

Sample	**Density**	**Grain size (μm)**	**Pore size (μm)**	**Residual Porosity (%)**	**Reference**
HEB_Zr	96.5±0.7	5.4±2	0.51±0.40	2.3	**This work**
HEB_Nb	97.4±0.3	10.9±4.6	0.51±0.42	1.5	**This work**
ZrB_2	98.3±0.8	20–30	3–4	5	**[18,35]**
TaB_2	94.0±0.4	10	0.5–3.0	5	**[18,35]**
TiB_2	~ 100	n.r.	n.r.	n.r.	**[20]**
HfB_2	97.6	~ 20	<5 μm	n.r.	**[22]**

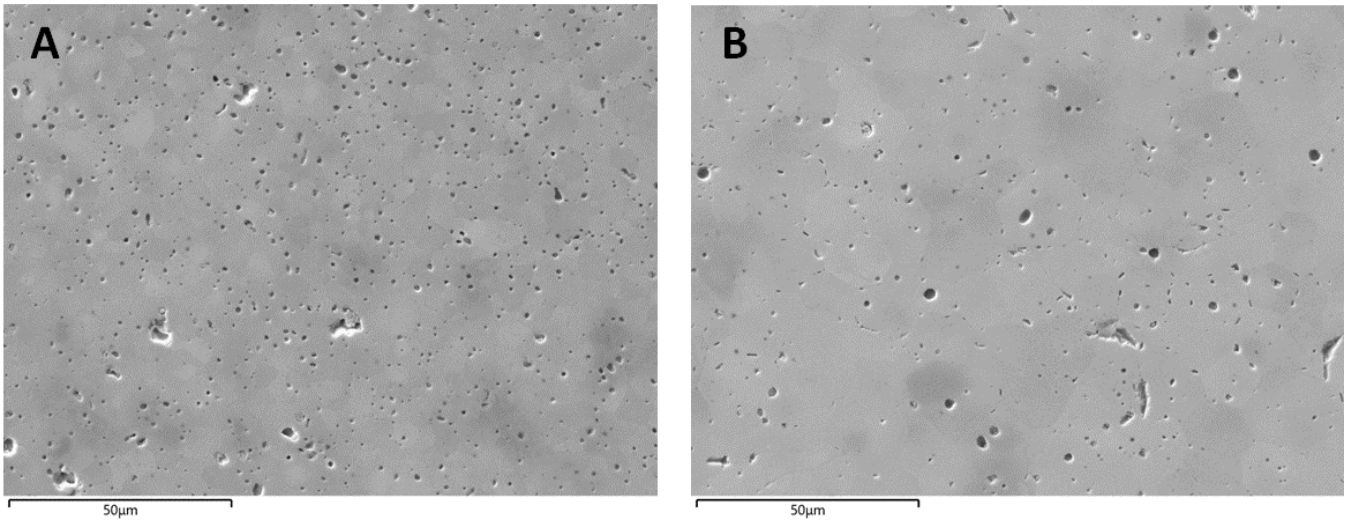

Figure 2: SE SEM image of (A) HEB_Zr and (B) HEB_Nb sample surfaces.

As surface texture significantly affects the optical properties, each sample was characterized by 3D optical profilometry in order to compare the intrinsic optical properties of the prepared materials. **Figure 3** show the areal surface maps and **Table 3** reports the average values of the areal height parameters measured on both samples, along with the corresponding standard deviation.

The surfaces of the analyzed systems show similar textural characteristics as highlighted by the quite close values of the parameter reported in **Table 2**. Both materials show low values of Sq and Sa, typical of reflective and smooth surfaces, even if slightly higher values were observed on the sample HEB_Nb. The presence of some surface porosities is highlighted by negative values of the Ssk parameter and by values of Sku > 3 as confirmed by the SEM analysis.

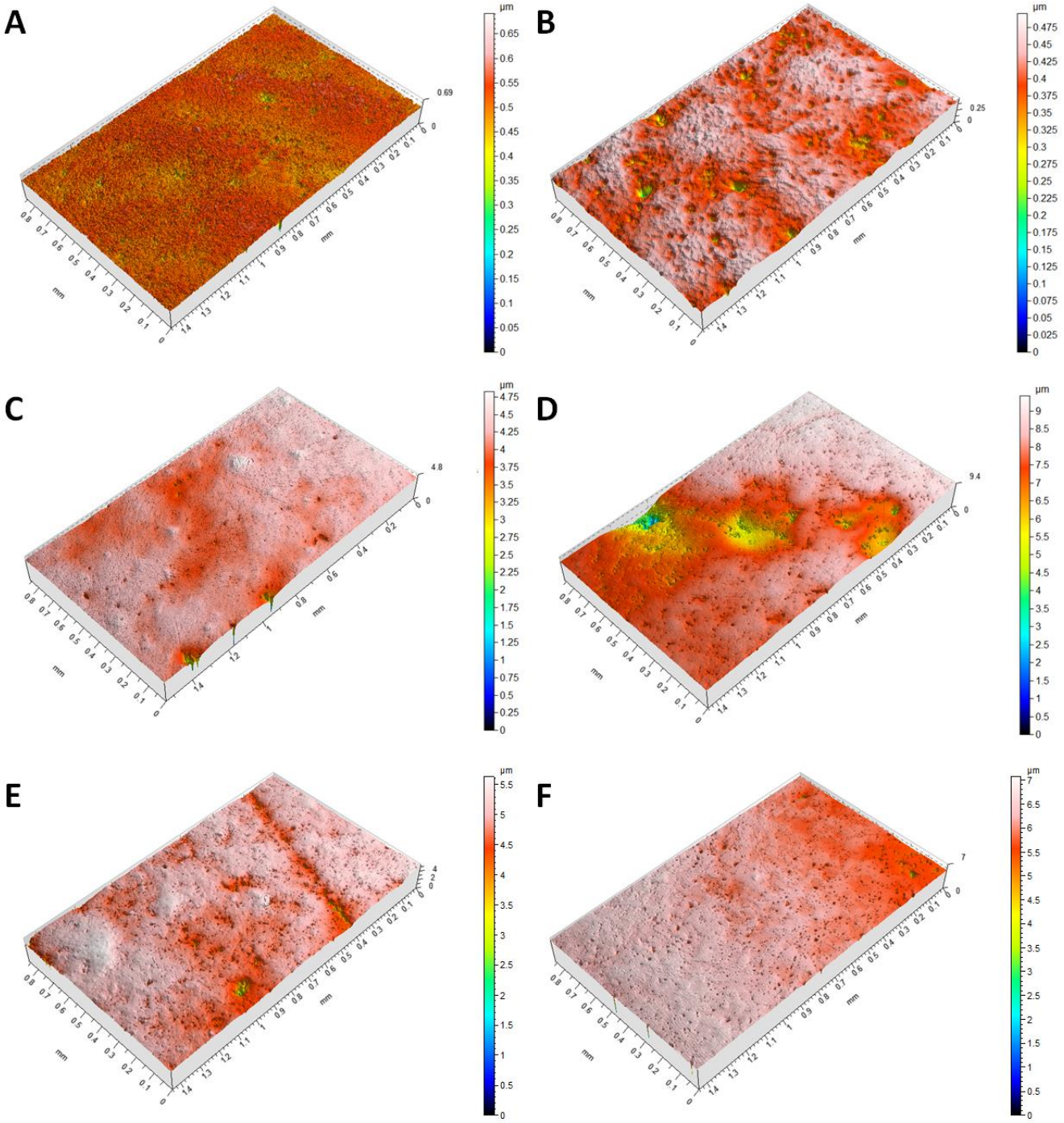

Figure 3*:* Surface texture of (A) HEB_Zr, (B) HEB_Nb, (C) ZrB_2, (D) TaB_2, (E) TiB_2, and (F) HfB_2, obtained by 3D optical profilometry. The height (z) of the surface was amplified by 10% compared to those in x and y.

Table 3. Average values and standard deviation of areal height parameters measured on HEB_Zr and HEB_Nb. Data of previously investigated binary borides produced by SHS-SPS, except for HfB_2 (reactive SPS), are also listed, for comparison.

	HEB_Zr	**HEB_Nb**	**ZrB_2 [20]**	**TaB_2 [20]**	**TiB_2 [20]**	**HfB_2 [22]**
Sq (μm)	0.030 ± 0.002	0.045 ± 0.05	0.44±0.11	0.884±0.069	0.50±0.20	0.49±0.30
Ssk	-3.83 ±0.59	-3.32 0.68	-7.1±1.1	-5.8±1.9	-7.2±2.2	-6.3±5.0
Sku	42.6 ± 9.4	32 ± 13	83±15	51±29	94±40	89±69
Sp (μm)	0.31 ± 0.014	0.12 ± 0.01	2.9±2.0	1.46±0.27	1.44±0.47	1.22±0.30
Sv (μm)	0.70 ±0.03	0.94 ± 0.43	9.6±2.6	12.9±3.0	10.6±3.7	12±7
Sz (μm)	1.01 ± 0.03	1.06 ± 0.43	12.5±4.6	14.3±2.8	12.0±4.1	13±7
Sa (μm)	0.02 ± 0.001	0.030 ± 0.008	0.211±0.028	0.440±0.042	0.237±0.057	0.249±0.062

To better evaluate the optical properties of HEB ceramics, the monolithic borides (ZrB_2, TaB_2, Tib_2 and HfB_2), previously investigated **[20,22]**, were also here considered and their surface topography and texture parameters were reported in **Figure 3** and **Table 3**.

Monolithic diborides show overall surface characteristics that are quite similar to those of HEBs, substantially characterized by a fine textured surface with the presence of large and relatively smooth defect porosities. The values of Sq and Sa measured on the monolith samples are, however, at least an order of magnitude higher than those collected on HEBs, suggesting greater surface irregularity most probably due to different surface preparation processes. Despite the differences in terms of Sa and Sq, previous studies **[20]** showed that the intrinsic optical properties of monolithic diborides are mainly related to their chemical composition and the morphological characteristics of the surface play a minor role.

3.3. Optical properties

Figure 4 shows the room-temperature spectral hemispherical reflectance of HEB samples in the region 0.3-16 μm wavelength. The spectra appear similar for both samples, with small differences lying within the experimental uncertainty. A net step-like behavior is evidenced, proving that also these high-entropy compounds, like the individual borides, are intrinsically spectrally selective. As expected, since optical

properties are strongly connected to the composition and crystal structure, the comparison with monolithic borides shows spectral differences with the latter one.

Figure 5 compares the reflectance curves of HEB_Zr and monolithic borides previously synthesized **[18,20,22]**. HEBs do not exhibit the local minima in the near infrared (1-3 um spectral range) shown by HfB_2, ZrB_2 and TiB_2 (**Figure 5b**) and due to bound-electron effects **[42]**. On the contrary, the steep risefront of HEB reflectance is similar, even if slightly shifted towards longer wavelengths, to that of TaB_2, and it only includes the free-electrons contribution **[42]**. For this reason, in the following discussion about optical properties, HEBs will be compared to TaB_2. The cutoff wavelength λ_c, defined as the wavelength where the reflectance falls to 50% of its maximum value **[43]** is 590 nm for HEB_Zr, 535 nm for HEB_Nb and 530 nm for TaB_2, respectively. For these purely step-like spectra, λ_c is connected to the plasma frequency ω_p **[42,44]**. A redshifted λ_c implies a smaller ω_p, and, in pure diborides, a smaller atomic mass of the metal ion **[44]**. If we define, for HEBs, a phenomenological "average atomic mass of metal ions", as the average of atomic masses of involved metal ions, weighted by their molar ratio, we can see that, interestingly, HEBs agree with the ω_p dependence on metal atomic mass cited above, even if they are far from the ideal single-composition and mono-crystalline materials considered in **[44]**.

In the mid-infrared 3-16 um, all the curves appear smooth (the feature around 5-7 um is an instrumental artifact due to unbalanced gases in the sample chamber) and asymptotically reaching 100% reflectance. The height of the infrared plateau is connected to the free-electrons lifetime **[44]**. Thus, it is decreased by surface or near-surface defects, like, for instance, pores or grain boundaries. However, the HEB samples have fewer surface defects than TaB_2, while grain size is lower in HEB_Zr and comparable in HEB_Nb (**Table 2**). On the other hand, in high-entropy systems the electron scattering can be enhanced due to the lattice distortions **[45]**, which appear, therefore, the most likely explanation of the lower slope in reaching the infrared reflectance plateau we observed in HEBs, in comparison to TaB_2 (**Figure 5c**).

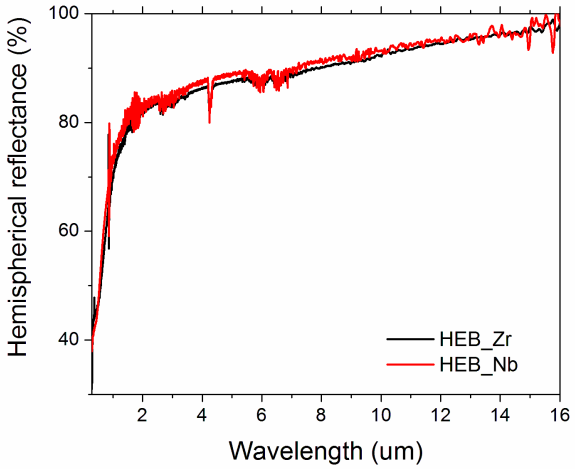

Figure 4: Hemispherical reflectance spectra of HEB_Zr and HEB_Nb samples.

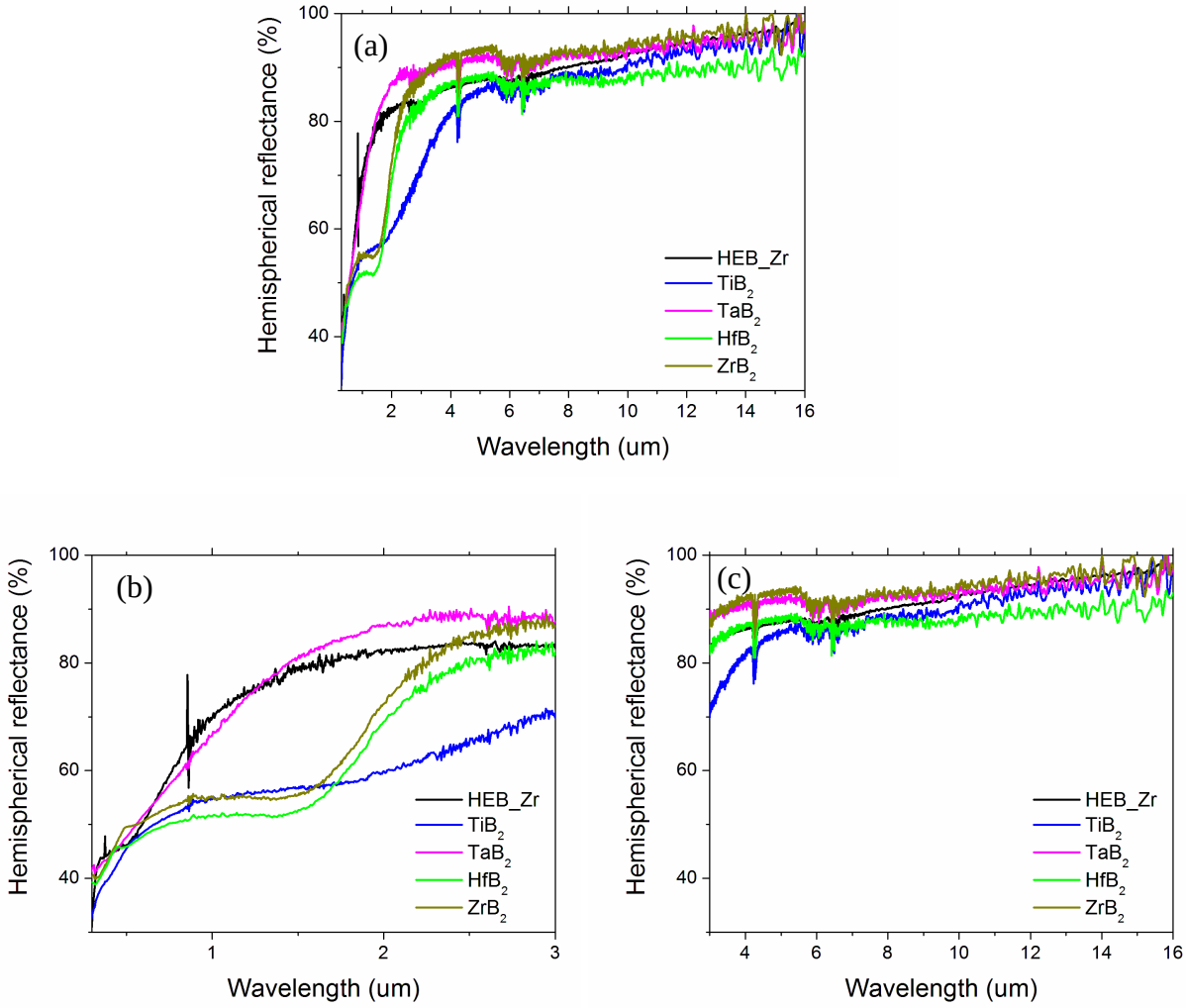

***Figure 5**:* Comparison of the hemispherical reflectance spectra of HEB_Zr and monolithic TiB_2, TaB_2, HfB_2 and ZrB_2 (from **[18,20,22]**). (a) Full spectral range and details of (b) 0.3-3 um range and (c) 3-16 um range.

Considering the optical parameters, solar absorptance α (Eq. 2), thermal emittance ε (Eq. 3) and spectral selectivity α/ε, **Figure 6** shows the calculated temperature-dependent values. Generally speaking, HEBs can be surely defined as low-emittance materials (ε=0.12~0.16 for HEB_Nb and ε=0.13~0.18 for HEB_Zr across the considered temperature range 800-1700 K). HEB_Zr and HEB_Nb show a small difference of about 0.02 absolute value, in both solar absorptance and emittance, with no appreciable differences in spectral selectivity. As observed in other individual (monolithic and composite) borides and, in general, in UHTCs, a higher solar absorptance is usually accompanied by a higher thermal

emittance **[19,46]**. Direct comparison is possible with TaB_2, which shows the same α value than HEB_Zr with a slightly lower ε, resulting, from the solely-optical point of view, slightly more performing. However, other characteristics impacting on the application must be considered. For instance, the relatively high specific weight of certain binary metal diborides, particularly TaB_2 and HfB_2, which possess high densities (12.6 and 11.2 g/cm³, respectively), could represent a drawback for some practical applications. Therefore, the partial replacement of Ta and Hf with alternative lighter transition metal elements (Zr, Nb, Mo, and Ti) provides a reduction of resulting density of the obtained ceramics, i.e. 8.52 (HEB_Zr) and 8.67 g/cm^3 (HEB_Nb). Furthermore, both Hf and Ta are in the list of 2020 Critical Raw Materials (CRMs) **[47]**, and the corresponding powders are relatively more expensive. Therefore, the possibility of substituting them with elements such as Zr and Mo (lighter, not CRM and cheaper), while keeping the resulting performances comparable, would represent an important target to achieve. In addition, these ceramics often exhibit superior hardness **[1,9,11]** and, most important for CSP applications, superior oxidation resistance **[1,13]** with respect to their individual constituents.

When the comparison with other monolithic borides is concerned, HEBs show a higher spectral selectivity than HfB_2 for T>1100 K and higher than ZrB_2 for T>1400K. The weakness point of HEBs is in the relatively low solar absorptance, which, however, can be increased using a proper surface texturing, e.g. by chemical etching **[28]** or laser machining **[21,48]**.

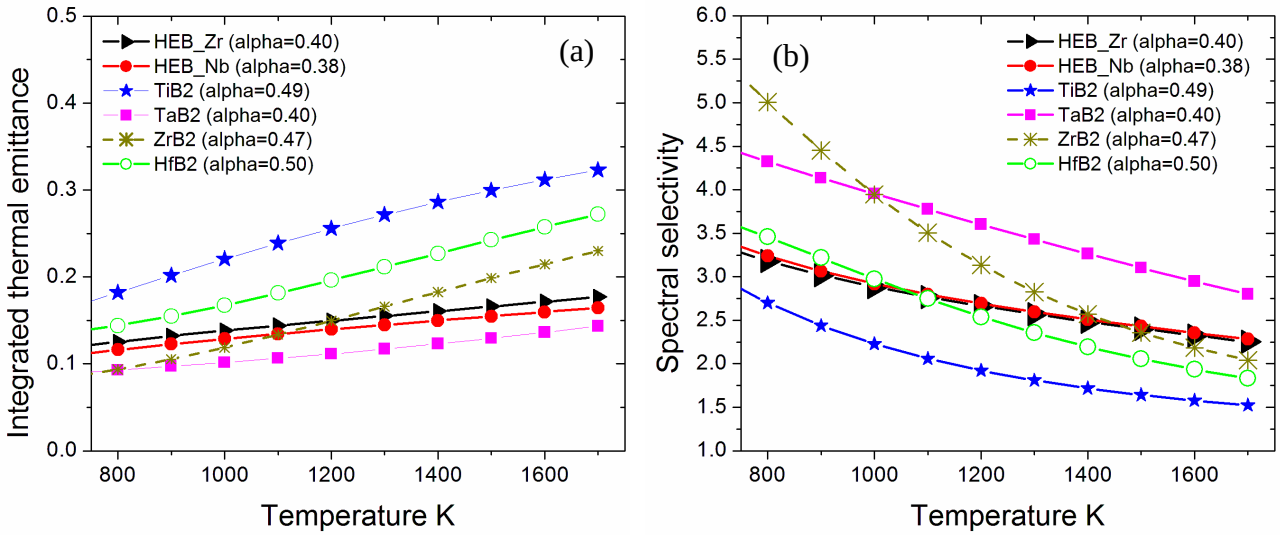

***Figure 6**:* Comparison of the calculated temperature-dependent thermal emittance (a) and spectral selectivity (b). The solar absorptance values are indicated in legend.

4. Conclusions

In this work, two high-entropy diboride bulk ceramics, with composition $(Hf_{0.2}Zr_{0.2}Ta_{0.2}Mo_{0.2}Ti_{0.2})B_2$ (labelled HEB_Zr) and $(Hf_{0.2}Nb_{0.2}Ta_{0.2}Mo_{0.2}Ti_{0.2})B_2$ (labelled HEB_Nb) have been successfully prepared by combining the SHS route, for powder synthesis, with the SPS technique, for their consolidation. The sintered samples have been characterized as for their microstructure and optical properties in the spectral range 0.3-16 μm wavelength, and compared with individual borides, obtained with the same SHS-SPS method, except for HfB_2 (reactive SPS). Step-like reflectance spectra, typical of intrinsic spectrally-selective materials, have been evidenced, with pure free-electrons contribution to optical properties. Optical parameters like solar absorptance, thermal emittance in the temperature range 800-1700K and spectral selectivity have been estimated from experimental spectra, to assess the HEBs' potential for high-temperature absorbers of solar radiation. Optical properties of the two investigated HEB compositions appear similar. Their main force point is the low thermal emittance, lower than 0.2 at all temperatures including 1700K, and the spectral selectivity remaining always higher than 2.2 (values to be compared with the most advanced solar absorber used in concentrating solar power plants to date, i.e. SiC, which shows ε~0.76-0.77 with no spectral selectivity **[17,49]**. On the other hand, their main weakness point is the solar absorptance value ~0.4, which, however, can be improved by proper texturing techniques, as we have demonstrated in other boride and carbide ultra-high temperature ceramics.

Acknowledgements

One of the authors (S.B.) performed his activity in the framework of the International PhD in Innovation Sciences and Technologies at the University of Cagliari, Italy. E.S thanks CNR-INO technicians Mr. M. D'Uva and Mr. M. Pucci for technical assistance.

The present work has been carried out in the framework of the ARCHIMEDES project sponsored by Regione Autonoma della Sardegna (Italy) – Fondo di Sviluppo e Coesione (FSC) 2014-2020 (Cod. RAS: RASSR88309, Cod. CUP: F76C18000980002).

References

[1] J. Gild, Y. Zhang, T. Harrington, S. Jiang, T. Hu, M.C. Quinn, W.M. Mellor, N. Zhou, K. Vecchio, J. Luo, High-Entropy Metal Diborides: A New Class of High-Entropy Materials and a New Type of Ultrahigh Temperature Ceramics, Sci Rep. 6 (2016) 37946. https://doi.org/10.1038/srep37946

[2] G. Tallarita, R. Licheri, S. Garroni, R. Orrù, G. Cao, Novel Processing Route for the Fabrication of Bulk High-Entropy Metal Diborides Scr. Mater. 158 (2019) 100-104 https://doi.org/10.1016/j.scriptamat.2018.08.039

[3] S. Barbarossa, R. Orrù, S. Garroni, R. Licheri, G. Cao, Ultra High Temperature High-Entropy Borides: Effect of Graphite Addition on Oxides Removal and Densification Behaviour, Ceram. Int. 47(5) (2021) 6220-6231 https://doi.org/10.1016/j.ceramint.2020.10.200

[4] L. Feng, W.G. Fahrenholtz, G.E. Hilmas, F. Monteverde, Effect of Nb content on the phase composition, densification, microstructure, and mechanical properties of high-entropy boride ceramics, J. Eur. Ceram. Soc. 41(1) (2021) 92-100 https://10.1016/j.jeurceramsoc.2020.08.058

[5] S. Akrami, P. Edalati, M. Fuji, K. Edalati, High-entropy ceramics: Review of principles, production and applications, Mater. Sci. Eng. R Rep. 146 (2021) 100644 https://doi.org/10.1016/j.mser.2021.100644

[6] H. Xiang, Y. Xing, F.-Z. Dai, H. Wang, L. Su, L. Miao, G. Zhang, Y. Wang, X. Qi, L. Yao, H. Wang, B. Zhao, J. Li, Y. Zhou, High-entropy ceramics: Present status, challenges, and a look forward, J. Adv. Ceram. 10(3) (2021) 385-441 https://doi.org/10.1007/s40145-021-0477-y

[7] Y. Zhang, W.-M., Guo, Z.-B. Jiang, Q.-Q. Zhu, S.-K. Sun, Y. You, K. Plucknett, H.-T. Lin, Dense high-entropy boride ceramics with ultra-high hardness, Scr. Mater. 164 (2019) 135-139. https://doi.org/10.1016/j.scriptamat.2019.01.021

[8] J. Gild, A. Wright, K. Quiambao-Tomko, M. Qin, J. A. Tomko, Md Shafkat bin Hoque, J. L. Braun, B. Bloomfield, D. Martinez, T. Harrington, K. Vecchio, P. E. Hopkins, J. Luo, Thermal conductivity and hardness of three single-phase high-entropy metal diborides fabricated by borocarbothermal reduction and spark plasma sintering. Ceram. Int. 2020, 46(5), 6906-6913. https://doi.org/10.1016/j.ceramint.2019.11.186

[9] Y. Zhang, S.K. Sun, W. Zhang, Y. You, W.M. Guo, Z.W. Chen, J.H. Yuan, H.T. Lin, Improved densification and hardness of high entropy diboride ceramics from fine powders synthesized via borothermal reduction process. *Ceram. Int.*, 46(9) (2020) 14299-14303. https://doi.org/10.1016/j.ceramint.2020.02.214

[10] S. Barbarossa, R. Orrù, V. Cannillo, A. Iacomini, S. Garroni, M. Murgia, G. Cao, Fabrication and Characterization of Quinary High Entropy-Ultra-High Temperature Diborides, Ceramics 4 (2021) 108–120. https://doi.org/10.3390/ceramics4020010

[11] Y. Zhang, Z.B. Jiang,, S.K. Sun, W.M. Guo, Q.S. Chen, J.X. Qiu, K. Plucknett, H.T. Lin, Microstructure and mechanical properties of high-entropy borides derived from boro/carbothermal reduction. J. Eur. Ceram. Soc., 39(13) (2019) 3920-3924. https://doi.org/10.1016/j.jeurceramsoc.2019.05.017

[12] H. Chen, H. Xiang, F.-Z. Dai, J. Liu, Y. Zhou, Porous high entropy $(Hf_{0.2}Zr_{0.2}Ta_{0.2}Nb_{0.2}Ti_{0.2})B_2$: A novel strategy towards making ultrahigh temperature ceramics thermal insulating, J. Mater. Sci. Technol. 35(10) (2019) 2404-2408 https://doi.org/10.1016/j.jmst.2019.05.059

[13] G. Tallarita, R. Licheri, S. Garroni, S. Barbarossa, R. Orrù, G. Cao High-Entropy Transition Metal Diborides by Reactive and Non-Reactive Spark Plasma Sintering: a comparative investigation J. Eur. Ceram. Soc. 40(4) (2020) 942-952 https://doi.org/10.1016/j.jeurceramsoc.2019.10.031

[14] L. Backman, J. Gild, J. Luo, E.J. Opila, Part II: Experimental verification of computationally predicted preferential oxidation of refractory high entropy ultra-high temperature ceramics, Acta Mater. 197 (2020) 81-90. https://doi.org/10.1016/j.actamat.2020.07.004

[15] C.-Y. He, X.-H. Gao, X.-L. Qiu, D.-M. Yu, H.-X., Guo, G. Liu, Scalable and Ultrathin High-Temperature Solar Selective Absorbing Coatings Based on the High-Entropy Nanoceramic AlCrWTaNbTiN with High Photothermal Conversion Efficiency Solar RRL 5(4) (2021) 2000790 https://doi.org/10.1002/solr.202000790

[16] C.-Y. He, X.-L. Qiu, D.-M. Yu, S.-S. Zhao, H.-X. Guo, G. Liu, X.-H. Gao, Greatly enhanced solar absorption via high entropy ceramic AlCrTaTiZrN based solar selective absorber coatings, J Materiomics 7(3) (2021) 460-469 https://doi.org/10.1016/j.jmat.2020.11.010

[17] E. Sani, L. Mercatelli, F. Francini, J.L. Sans, D. Sciti, Ultra-refractory ceramics for high-temperature solar absorbers. Scr. Mater., 65(9) (2011) 775-778. https://doi.org/10.1016/j.scriptamat.2011.07.033

[18] E. Sani, L. Mercatelli, M. Meucci, A. Balbo, C. Musa, R. Licheri, R. Orrù, G. Cao, Optical properties of dense zirconium and tantalum diborides for solar thermal absorbers, Renew. Energy 91 (2016) 340–346, https://doi.org/10.1016/j. renene.2016.01.068

[19] E. Sani, L. Mercatelli, M. Meucci, A. Balbo, L. Silvestroni, D. Sciti, Compositional dependence of optical properties of zirconium, hafnium and tantalum carbides for solar absorber applications. Sol. Energy, 131 (2016) 199-207. https://doi.org/10.1016/j.solener.2016.02.045

[20] E. Sani, M. Meucci, L. Mercatelli, A. Balbo, C. Musa, R. Licheri, R. Orrù, G. Cao, Titanium diboride ceramics for solar thermal absorbers. Sol. Energy Mater. Sol. Cells, 169 (2017) 313-319 https://doi.org/10.1016/j.solmat.2017.05.038

[21] E. Sani, D. Sciti, L., Silvestroni, A. Bellucci, S. Orlando, D.M. Trucchi, Tailoring optical properties of surfaces in wide spectral ranges by multi-scale femtosecond-laser texturing: A case-study for TaB_2 ceramics. Opt. Mater., 109 (2020) 110347 https://doi.org/10.1016/j.optmat.2020.110347

[22] C. Musa, R. Licheri, R. Orrù, G. Cao, A. Balbo, F. Zanotto, L. Mercatelli, E. Sani, Optical characterization of hafnium boride and hafnium carbide-based ceramics for solar energy receivers. Sol. Energy, 169 (2018) 111-119. https://doi.org/10.1016/j.solener.2018.04.036

[23] X.L. Qiu, X.H. Gao, C.Y. He, B.H. Chen, G. Liu, Structure, optical simulation and thermal stability of the HfB_2-based high-temperature solar selective absorbing coatings. RSC adv. 9(51) (2019) 29726-29733. https://doi.org/10.1039/c9ra05014k

[24] X.L. Qiu, X.H. Gao, T.H. Zhou, B.H. Chen, J.Z. Lu, H.X. Guo, X.T. Li, G., Liu, Structure, thermal stability and chromaticity investigation of TiB_2 based high temperature solar selective absorbing coatings. Sol. Energy, 181 (2019) 88-94. https://doi.org/10.1016/j.solener.2019.01.068

[25] X.L. Qiu, X.H. Gao, C.Y. He, G. Liu, Enhanced thermal stability of the TiB_2–ZrB_2 composite ceramic based high temperature spectrally selective absorber coatings: optical properties, failure analysis and chromaticity investigation. Opt. Mater. 100 (2020) 109666. https://doi.org/10.1016/j.optmat.2020.109666

[26] P.R. Kumar, M.A. Hasan, A. Dey, B. Basu, Development of ZrB_2-Based Single Layer Absorber Coating and Molten Salt Corrosion of Bulk ZrB_2–SiC Ceramic for Concentrated Solar Power Application. J. Phys. Chem. C 125(24) (2021) 13581-13589. https://doi.org/10.1021/acs.jpcc.1c01984

[27] R.K. Poobalan, M.P. Singh, B. Basu, Probing the spectrally selective property of NbB_2-based tandem absorber coating for concentrated solar power application. J. Am. Ceram. Soc. 105(2) (2022) 1136-1148. https://doi.org/10.1111/jace.18143

[28] L. Silvestroni, D. Sciti, L. Zoli, A. Balbo, F. Zanotto, R. Orrù, R. Licheri, C. Musa, L. Mercatelli, E. Sani, An overview of ultra-refractory ceramics for thermodynamic solar energy generation at high temperature. Renew. Energy 133 (2019) 1257-1267 https://doi.org/10.1016/j.renene.2018.08.036

[29] IRENA 2018, "Global Energy Transformation: A Roadmap to 2050 (2018 Edition)," Int. Renew. Energy Agency, Abu Dhabi. ISBN : 978-92-9260-059-4

[30] Heliogen and Bloom Energy Lead the Way to Produce Low-Cost, Green Hydrogen Following Successful Demonstration. Bloomenergy Web site. https://www.bloomenergy.com/news/heliogen-and-bloom-energy-lead-the-way-to-produce-low-cost-green-hydrogen-following-successful-demonstration/, 2021 (accessed 31 August, 2022)

[31] R. Thonig, J. Lilliestam, Concentrating Solar Technology Policy Should Encourage High Temperatures and Modularity to Enable Spillovers. AIP Conf. Proc. (2021);in review

[32] P. Furler, D. Marxer, J. Scheffe, D. Reinalda, H. Geerlings, C. Falter, V. Batteiger, A. Sizmann; A. Steinfeld, Solar kerosene from H_2O and CO_2. AIP Conf. Proc. 1850 (2017) 100006 https://doi.org/10.1063/1.4984463

[33] C. Falter, N. Scharfenberg, A. Habersetzer, Geographical potential of solar thermochemical jet fuel production, Energies 13 (2020) 802. https://doi.org/10.3390/en13040802

[34] C. Falter, A. Sizmann. Solar Thermochemical Hydrogen Production in the USA. Sustainability 13 (2021) 7804 https://doi.org/10.3390/su13147804

[35] R. Licheri, C. Musa, R. Orrù, G. Cao, D. Sciti, L. Silvestroni, Bulk monolithic zirconium and tantalum diborides by reactive and non-reactive spark plasma sintering, J. Alloys Compd. 663 (2016) 351–359, https://doi.org/10.1016/j. jallcom.2015.12.096

[36] F.L. Matthews, R. Rawlings Composite Materials: Engineering and Science. Chapman & Hall, Great Britain; 1994. ISBN: 9781855734739

[37] Standard Tables for Reference Solar Spectral Irradiances: Direct Normal and Hemispherical on 37° Tilted Surface, Active Standard ASTM G173. ASTM G173 – 03 (2012)

[38] N. Azzali, M. Meucci, D. Di Rosa, L. Mercatelli, L. Silvestroni, D. Sciti, E. Sani, Spectral emittance of ceramics for high temperature solar receivers. Sol. Energy, 222 (2021) 74-83. https://doi.org/10.1016/j.solener.2021.05.019

[39] S.K. Mishra, L.C. Pathak, Effect of carbon and titanium carbide on sintering behavior of zirconium diboride, J. Alloys Compd. 465 (2008) 547–555. https://doi.org/10.1016/j.jallcom.2007.11.004

[40] V. Zamora, M. Nygren, F. Guiberteau, A.L. Ortiz, Effect of graphite addition on the spark-plasma sinterability of ZrB_2 and ZrB_2–SiC ultra-high-temperature ceramics, Ceram. Int. 40 (2014) 11457-11464. https://doi.org/10.1016/j.ceramint.2014.03.130

[41] M.A. Kuzenkova, P.S. Kislyi, O.V. Zaverukha, Y.B. Kus'ma, Structure and properties of zirconium diboride-tungsten alloys, Sov. Powder Metall. Met. Ceram. 10 (1971) 879–883. https://doi.org/10.1007/BF00793999.

[42] C.F. Bohren, D.R. Huffman, Absorption and Scattering of Light by Small Particles, Wiley Interscience, New York (1983)

[43] E. Sani, L. Mercatelli, J.L. Sans, L. Silvestroni, D. Sciti, Porous and dense hafnium and zirconium ultra-high temperature ceramics for solar receivers. Opt. Mater. 36(2), (2013) 163-168. https://doi.org/10.1016/j.optmat.2013.08.020

[44] H. Xiang, F. Dai, Y. Zhou, Theoretical insight into the solar thermal absorption property of ultra-high temperature ceramics TMB_2 (TM= Ti, Zr, and Hf). Sol. Energy Mater. Sol. Cells, 225 (2021) 111032 https://doi.org/10.1016/j.solmat.2021.111032

[45] M.J. Haché, C. Cheng, Y. Zou, Nanostructured high-entropy materials. J. Mater. Res. 35(8) (2020) 1051-1075 https://doi.org/10.1557/jmr.2020.33

[46] L. Zoli, S. Failla, E. Sani, D. Sciti, Novel ceramic fibre-Zirconium diboride composites for solar receivers in concentrating solar power systems. Compos. B. Eng., 242 (2022) 110081 https://doi.org/10.1016/j.compositesb.2022.110081

[47] Communication from the Commission to the European Parliament, the Council, the European Economic and Social Committee and the Committee of the Regions - Critical Raw Materials Resilience: Charting a Path towards greater Security and Sustainability. An official Web site of the European Union. Document 52020DC0474. https://eur-lex.europa.eu/legal-content/EN/TXT/?uri=CELEX:52020DC0474, 2022 (accessed 31 August, 2022)

[48] D. Sciti, D.M. Trucchi, A. Bellucci, S. Orlando, L. Zoli, E. Sani, Effect of surface texturing by femtosecond laser on tantalum carbide ceramics for solar receiver applications, Sol. Energy Mater. Sol. Cells, 161 (2017) 1-6. https://doi.org/10.1016/j.solmat.2016.10.054

[49] D. Sciti, L. Silvestroni, L. Mercatelli, J.L. Sans, E. Sani, Suitability of ultra-refractory diboride ceramics as absorbers for solar energy applications, Sol. Energy Mater. Sol. Cells, 109 (2013) 8-16. https://doi.org/10.1016/j.solmat.2012.10.004